

Fluid pipes

By MATTHEW J. HANCOCK¹ AND JOHN W. M. BUSH²

¹Department of Civil and Environmental Engineering, Massachusetts Institute of Technology,
77 Massachusetts Avenue, Cambridge, MA 02139, USA

²Department of Mathematics, Massachusetts Institute of Technology, 77 Massachusetts Avenue,
Cambridge, MA 02139, USA

(Received 8 March 2001 and in revised form 19 March 2002)

We present the results of a combined theoretical and experimental investigation of laminar vertical jets impinging on a deep fluid reservoir. We consider the parameter regime where, in a pure water system, the jet is characterized by a stationary field of capillary waves at its base. When the reservoir is contaminated by surfactant, the base of the jet is void of capillary waves, cylindrical and quiescent: water enters the reservoir as if through a rigid pipe. A theoretical description of the resulting fluid pipe is deduced by matching extensional plug flow upstream of the pipe onto entry pipe flow within it. Theoretical predictions for the pipe height are found to be in excellent accord with our experimental results. An analogous theoretical description of the planar fluid pipe expected to arise on a falling fluid sheet is presented.

1. Introduction

The flow of interest may be readily observed in a kitchen sink. When the volume flux exiting the tap is such that the falling stream has a diameter of 2–3 mm, obstructing the stream with a finger at a distance of several centimetres from the tap gives rise to a stationary field of varicose capillary waves upstream of the finger. If the finger is dipped in liquid detergent before insertion into the stream, the capillary waves begin at some critical distance above the finger, below which the stream is cylindrical. Closer inspection reveals that the surface of the jet's cylindrical base is quiescent. We here develop a description of the dynamics responsible for this curious phenomenon.

The dynamics of laminar fluid jets have been studied extensively (Marshall & Pigford 1947; Scriven & Pigford 1959; Duda & Vrentas 1967; Brun & Lienhard 1968; Lienhard 1968; Clarke 1968, 1969; Kaye & Vale 1969; Petrie 1979; Adachi 1987; González-Mendizabal, Olivera-Fuentes & Guzmán 1987) and the propagation of capillary waves on jets has become a textbook example (Drazin & Reid 1981; Bird, Armstrong & Hassager 1987). Rayleigh (1879, 1892) examined the stability of a cylindrical fluid jet in the absence of gravity, and demonstrated that axisymmetric varicose perturbations with wavelength λ greater than the jet circumference $2\pi a$ grow exponentially and lead to jet breakup, while those with $\lambda < 2\pi a$ are neutrally stable and propagate along the jet. Anno (1977) extended Rayleigh's theory to describe capillary waves on free-falling vertical jets, and demonstrated that a stationary field of neutrally stable varicose capillary waves exists on the jet when the phase speed matches the local jet speed. While the influence of fluid viscosity on the shape of such water jets is negligible, viscous damping has a significant impact on the neutrally stable waves (Awati & Howes 1996); specifically, the wave amplitude decreases exponentially with distance from the disturbance source.

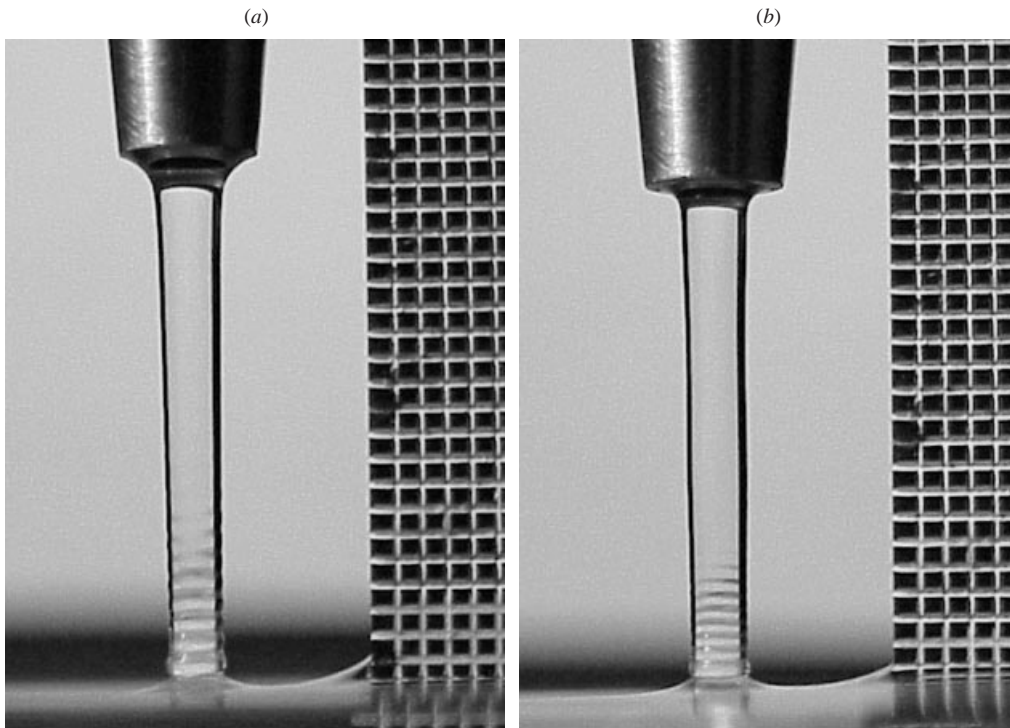


FIGURE 1. Water jets impinging on a pure water reservoir when (a) $Q = 3.2 \text{ cm}^3 \text{ s}^{-1}$, (b) $Q = 4.6 \text{ cm}^3 \text{ s}^{-1}$. The grid on the right is millimetric.

When an axisymmetric fluid jet impinges on a deep reservoir of the same fluid, a stationary field of varicose capillary waves is excited by the impact and may be observed near the base of the jet (figure 1). When the reservoir is contaminated by surfactant, so that its surface tension is less than that of the impinging jet, the flow structure is dramatically altered (figure 2). First, the varicose capillary waves are suppressed at the base of the jet, but resume at some distance above the reservoir. Second, the region of the jet surface that is void of capillary waves is entirely quiescent. The jet enters the reservoir as if through a rigid pipe, henceforth referred to as the ‘fluid pipe’. Fluid pipes were first reported in an experimental study of gas absorption by liquid jets impinging on a fluid reservoir (Cullen & Davidson 1957); however, a consistent theoretical description of the fluid pipe has yet to be presented.

In §2, we present a physical picture of the fluid pipe, and a simple scaling result for its vertical extent. Our experimental procedure is outlined in §3. In §4, we review the dynamics of falling jets and the field of capillary waves which they may support. In §5, we develop a detailed theoretical description of the fluid pipe. Our model yields a prediction for the pipe height which is tested experimentally.

2. Physical picture

We consider the system illustrated in figure 3. A laminar vertical water jet of viscosity ν , density ρ and surface tension σ_0 is generated by releasing a volume flux Q from an outlet of radius a_N . The characteristic Reynolds number $Q/(a_N\nu)$ is large. The jet evolves under the influence of gravitational acceleration $g\hat{z}$ (\hat{z} is the unit vector pointing downward) and impinges on a deep surfactant-laden reservoir characterized by a

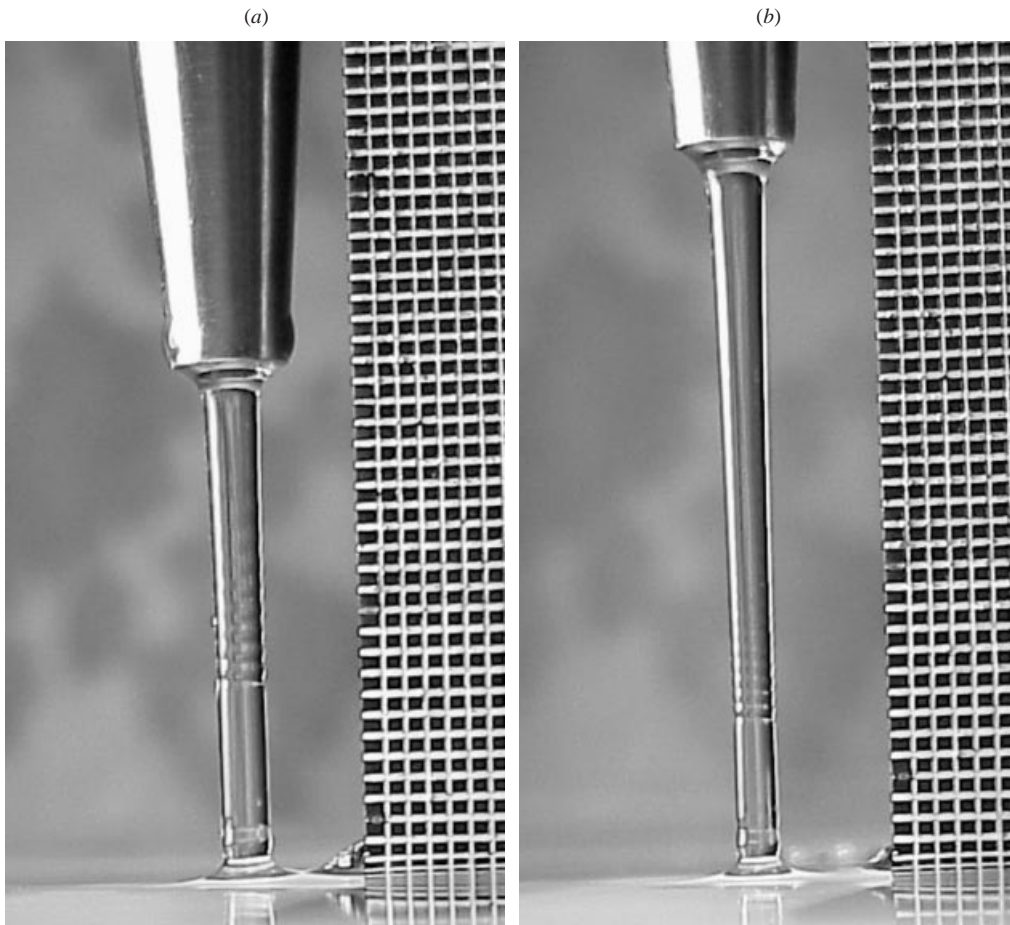


FIGURE 2. Stagnant fluid pipes at the base of water jets impinging on a reservoir contaminated with Ivory dish detergent when (a) $Q = 3.2 \text{ cm}^3 \text{ s}^{-1}$ and (b) $Q = 2.6 \text{ cm}^3 \text{ s}^{-1}$. Capillary waves are suppressed on the fluid pipe, but resume above it.

surface tension $\sigma_1 < \sigma_0$. The concomitant surface-tension gradient draws surfactant up the jet until a balance is established between viscous and Marangoni stresses at the jet surface. Surfactants generally impart an effective elasticity to an interface (Levich 1962) and so serve to suppress capillary waves (Lucassen-Reynders & Lucassen 1969; Hansen & Ahmad 1971). Consequently, capillary waves are suppressed on the pipe but resume above it. The extensional surface motions associated with the plug flow are also suppressed by the vertical Marangoni stress, giving rise to a stagnant surface at the base of the jet, a fluid pipe of radius a and height H . In our detailed theoretical description of §5, we model the flow in the fluid pipe by matching the extensional plug flow above the pipe onto entry pipe flow within it.

In laminar entry pipe flow, a boundary layer of thickness $\delta(z)$ grows along the sides of the pipe throughout the 'inlet region', until its thickness becomes comparable to the pipe radius. Mohanty & Asthana (1978) calculate the streamwise extent of the inlet region as $L_F \sim 0.072 a Re$, where $Re = aV/\nu$ is the Reynolds number based on the entry speed V and the pipe radius a . In our experiments, $a \sim 0.1 \text{ cm}$, $V \sim (30\text{--}100) \text{ cm s}^{-1}$, and $\nu = 0.01 \text{ cm}^2 \text{ s}^{-1}$; hence, $Re \sim 300$ and $L_F \sim (2\text{--}7) \text{ cm}$. Since

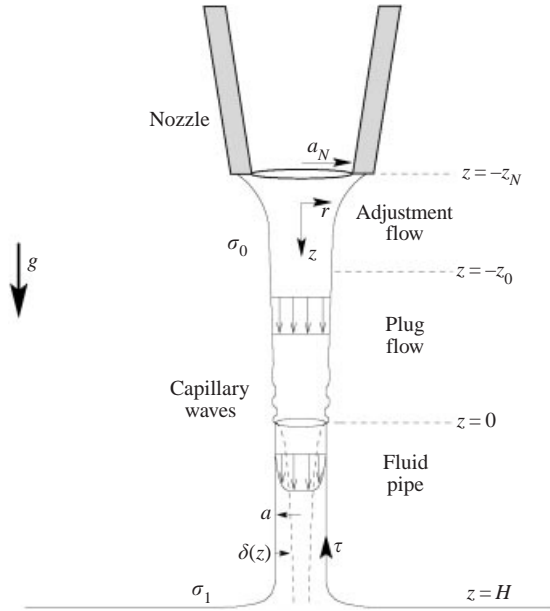


FIGURE 3. A schematic illustration of the flow of interest, which may be described in terms of three distinct regions: (a) adjustment flow ($-z_N < z < -z_0$); (b) extensional plug flow ($-z_0 < z < 0$); and (c) the fluid pipe ($0 < z < H$).

the maximum height H of the fluid pipes observed in our experiments was 2 cm, the flow within the fluid pipe may be adequately described as that within the inlet region of entry pipe flow.

We proceed by deducing a simple scaling which indicates the dependence of the fluid pipe height H on the governing system parameters. Balancing viscous and Marangoni stresses on the pipe surface yields

$$\rho v \frac{V}{\delta_H} \sim \frac{\Delta\sigma}{H}, \quad (2.1)$$

where $\Delta\sigma = \sigma_0 - \sigma_1$ and δ_H is the boundary layer thickness at the base of the fluid pipe. We assume that the boundary layer thickness increases with distance z from the inlet according to

$$\frac{\delta}{a} \sim \left(\frac{vz}{a^2 V} \right)^{1/2} = \left(\frac{z}{a Re} \right)^{1/2} \quad (2.2)$$

(Schlichting 1987). Substituting (2.2) into (2.1) yields

$$\frac{H}{a} \sim \frac{1}{Re} \frac{(\Delta\sigma)^2}{(\rho v V)^2} = \frac{Re}{W_d^2}, \quad (2.3)$$

where $W_d = \rho a V^2 / \Delta\sigma$ is the dynamic Weber number. In dimensional form, we thus obtain

$$H \sim \frac{(\Delta\sigma)^2}{\rho \mu V^3} = \frac{(\Delta\sigma)^2 \pi^3 a^6}{\rho \mu Q^3}. \quad (2.4)$$

The pipe height increases with the surface tension differential and pipe radius, and decreases with fluid viscosity and volume flux. A complete theoretical description of the fluid pipe, which requires consideration of the combined influence of gravity and the free pipe surface on the boundary layer dynamics, is presented in § 5.

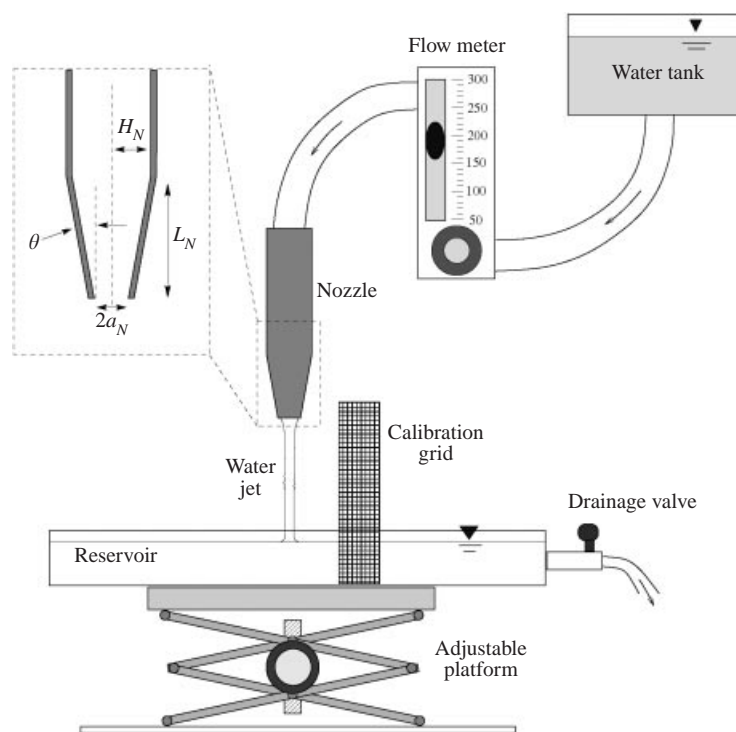


FIGURE 4. A schematic illustration of the experimental apparatus. The nozzle specifications ($L_N = 3.0$ cm, $H_N = 0.50$ cm, $a_N = 0.15$ cm, $\theta = 6.7^\circ$) were chosen to minimize the extent of the adjustment region.

3. Experimental method

The experimental apparatus is illustrated in figure 4. Distilled water is gravity-fed from a tank and discharges from a nozzle of radius a_N into a reservoir. The flow rate Q is measured using a rotameter in series with the flow. The reservoir is mounted on an adjustable platform which allows the distance between the reservoir and nozzle to be varied. The reservoir has an adjustable drain, which makes it possible to keep the water level constant, and so prevent the overflow of surfactant. Images of the jet were taken with a digital camera, then loaded into Matlab, where the jet profile, capillary wavelengths and fluid pipe height could be measured using Matlab's Image Processing Toolbox. A millimetric grid placed in the plane of the jet allowed calibration of distances in the digital images.

Measurements of the capillary wave field were made at the base of jets impinging on a distilled water reservoir. Fluid pipes were generated by adding one of a variety of surfactants (including Tide, Ivory, sodium dodecyl sulphate (SDS) and a superwetting agent) to the reservoir in sufficient quantities to saturate the horizontal surface and so minimize its surface tension. The fluid pipe experiments were performed with layers sufficiently deep (1–2 cm) that the pipe structure was independent of layer depth. Typical flow rates were 2 to 5 cm³ s⁻¹, and nozzle-to-reservoir distances 1 to 6 cm. Measurements of the surface tensions of the jet and reservoir were made using a Kruss K10 surface tensiometer, which has an accuracy of 0.1%. The surface tensions in our experiments ranged from 26 to 72 dyn cm⁻¹. The surface tension of the source fluid, σ_0 , varied between 68 and 72 dyn cm⁻¹, with a mean value of 70.5 dyn cm⁻¹.

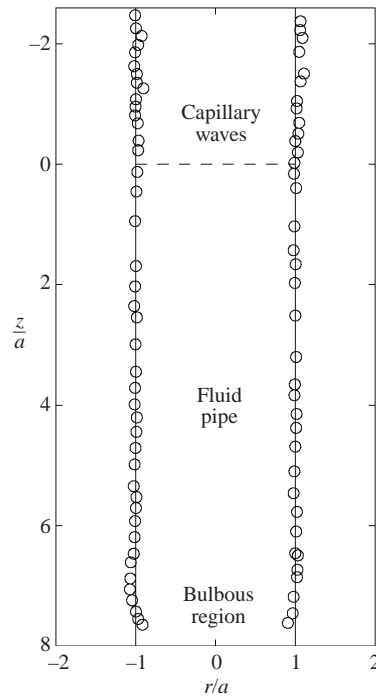


FIGURE 5. A typical profile of a water jet impinging on a reservoir contaminated with Ivory detergent. The radius of the fluid pipe is constant within the experimental error indicated by the radii of the circles. Capillary waves are evident above the pipe, while an underlying bulbous region joins the jet to the reservoir. Here $a = 0.11$ cm and $Q = 2.55$ cm³ s⁻¹.

This range indicates the degree of contamination of the source fluid by contact with the teflon tubing and flow meter. Finally, the surface tension differential $\Delta\sigma$ took mean values of 26.3 and 31.1 dyn cm⁻¹ for reservoirs saturated with Ivory and Tide detergents, respectively.

Figure 2 makes clear that the top of the fluid pipe is well-defined, while its base is marked by a bulbous region where the jet matches onto the reservoir. A characteristic pipe profile is illustrated in figure 5, where three distinct regions are apparent: the fluid pipe, the overlying capillary waves, and the underlying bulbous region. The radius of the fluid pipe was found to be constant within experimental error (approximately 1%). For both clean and contaminated reservoirs, the vertical extent of the bulbous region was found to decrease with flow rate in a manner expected for capillary waves; however, it was typically two to three times larger than the wavelength expected for capillary waves on a jet with surface tension corresponding to that of the reservoir, and was presumably influenced by the complex flow at the pipe's base. In the experimental measurements reported in § 5, the pipe base was taken to be the middle of the bulbous region; the errors in pipe height correspond to the half-height of the bulbous region.

The absence or presence of surface motions on the fluid pipe was made clear by sprinkling lycopodium powder onto the surface of the reservoir prior to initiation of the jet. When the jet was initiated, the powder was drawn up the pipe until an equilibrium state was achieved. A strictly quiescent pipe surface was observed only for surfactants containing a 'sparingly soluble' (that is, nearly insoluble) component (Porter 1994), specifically the commercial detergents Tide and Ivory. For the soluble surfactants examined, including SDS, the pipe surface was marked by weak circulation

patterns. Similarly, when the surface tension of the reservoir was reduced by the addition of alcohol (either ethanol or methanol), an unsteady pipe-like structure was observed. In our theoretical developments, we restrict our attention to the case of stationary fluid pipes.

4. Base flow

Our theoretical description of the fluid pipe requires that we match the extensional plug flow above the pipe onto entry plug flow within it. We thus proceed by describing the extensional plug flow, referred to as the base flow, as well as the field of capillary waves which it supports.

The base flow consists of a steady, laminar, axisymmetric jet falling from a reference level $z = -z_0$ (figure 3). We assume that the jet is in free-fall and has a plug profile $\mathbf{u} = U(z)\hat{\mathbf{z}}$ to leading order. The jet has an axial length scale $L \sim 1$ cm, a radial scale $a_0 \sim 0.1$ cm, and characteristic speed $U \sim 30$ cm s⁻¹. Since the corresponding Reynolds number is large, the flow may be adequately described as inviscid to leading order.

Since the flow is steady, the volume flux Q across any cross-section is constant:

$$Q = 2\pi \int_0^a U r \, dr = \pi a^2 U = \pi a_0^2 U_0, \quad (4.1)$$

where $a = a(z)$ is the radius of the jet, and U_0 is the axial speed at the reference level $z = -z_0$ where $a = a_0$. Since the flow is effectively inviscid and has a plug profile, Bernoulli's Principle may be applied to yield

$$\frac{U^2}{2} + \frac{\sigma}{\rho a} - gz = \frac{U_0^2}{2} + \frac{\sigma}{\rho a_0} + gz_0 \quad (4.2)$$

(e.g. Cullen & Davidson 1957). Note that the jet radius is assumed to be slowly varying in z so that the relevant pressure jump across the interface is $\sigma \nabla \cdot \mathbf{n} = \sigma/a(z)$ to leading order. Rearranging (4.2) yields

$$\frac{U}{U_0} = \sqrt{1 + \Pi - \frac{2}{W_0} \left(\frac{a_0}{a} - 1 \right)}, \quad (4.3)$$

where $\Pi = 2g(z + z_0)/U_0^2$ is an inverse Froude number and $W_0 = \rho a_0 U_0^2 / \sigma$ is the Weber number. Combining (4.1) and (4.3) yields

$$\frac{a}{a_0} = \left(1 + \Pi - \frac{2}{W_0} \left(\frac{a_0}{a} - 1 \right) \right)^{-1/4}. \quad (4.4)$$

In the zero surface tension limit, (4.3) and (4.4) become

$$\frac{U}{U_0} = \sqrt{1 + \Pi}, \quad \frac{a}{a_0} = (1 + \Pi)^{-1/4}. \quad (4.5)$$

The close agreement between the predicted radial profiles (4.4) and (4.5) at sufficient distance from the nozzle is evident in figure 6, and suggests that (4.5) is sufficient to describe the jet profile in the region of interest.

The influence of the rigid nozzle walls on the jet profile (see Brun & Lienhard 1968; McCarthy & Malloy 1974; González-Mendizabal *et al.* 1987; and references therein) extends a distance L_A from the source at $z = -z_N$. In order for the jet profiles to be adequately described by the inviscid theory, the reference level $z = -z_0$ must

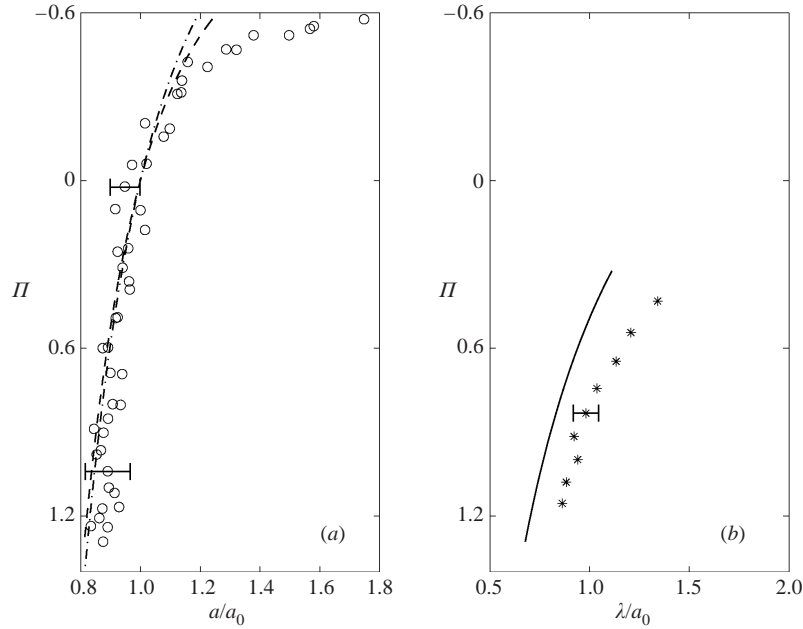


FIGURE 6. The form of a water jet with $Q = 1.86 \text{ cm}^3 \text{ s}^{-1}$, $a_0 = 0.110 \text{ cm}$, $W_0 = \rho a_0 U_0^2 / \sigma_0 = 3.71$, and nozzle to reservoir distance of 2.7 cm. (a) The observed dependence (\circ) of dimensionless jet radius a/a_0 on dimensionless height $\Pi = 2g(z + z_0)/U_0^2$. The theoretical jet profiles deduced by including ((4.4); dash-dot line) and neglecting ((4.5); dashed line) the influence of surface tension are also shown. (b) The observed dependence ($*$) of dimensionless capillary wavelength λ/a_0 on height. The theoretical prediction for this dependence (A 5) appears as a solid line. Characteristic error bars are shown.

be chosen below the adjustment region; $z_N - z_0 > L_A$. The only way to determine precisely the extent of the adjustment region is to measure velocity profiles within the jet; in the absence of such measurements, we were obliged to rely on previous predictions for the adjustment length. Brun & Lienhard 1968 estimate that for a cylindrical nozzle, $L_A/a = 0.1 Re$; however, it has also been shown that tapering the nozzle substantially reduces the extent of the adjustment length L_A (Brun & Lienhard 1968; McCarthy & Malloy 1974). Consequently, the nozzle used in our experiments was tapered near its exit in a manner detailed in figure 4.

Duda & Vrentas (1967) developed a theoretical model describing a vertical laminar liquid jet issuing from a cylindrical nozzle for the case where the initial jet profile is parabolic. The experimental results of González-Mendizabal *et al.* (1987) were consistent with Duda & Vrentas' theory, but also made clear that the inviscid model (4.4) provides an excellent description of the jet profile at sufficient distance from the nozzle exit region. Radial profile data from one of our experiments are presented in figure 6, and are well-described by (4.4) and (4.5) at sufficient distance from the source, specifically, beyond 4 to 7 nozzle radii. This length was typical in the parameter regime examined, and taken to be the adjustment length L_A in our experimental study. The scatter in the jet profile data evident at the base of the jet results from the distortion of the jet by capillary waves. A comprehensive data set for jet profiles in the absence of capillary waves is presented in González-Mendizabal *et al.* (1987).

The theory of capillary waves on falling jets is well-developed (Anno 1977), and is reviewed for the sake of completeness in Appendix A. The predicted dependence of

capillary wavelength λ on the governing parameters is given in (A 5). As there appears to be a scarcity of supporting experimental data, we undertook an experimental test of the capillary wave theory. Figure 6(b) shows the results of a typical experiment in which capillary wavelengths are plotted as a function of height. The error bars reflect the uncertainties introduced by the light scattered from the wave field. The data indicate that the simple linear theory provides a reasonable description of the data. The observed discrepancy probably results from the influence of nonlinear effects on the wave field. A more extensive data set indicating the observed dependence of λ on Π and W_0 is presented in Appendix A.

5. Fluid pipe

We proceed by deriving an approximate solution to the flow in the fluid pipe by adapting established models of entry flow into a rigid pipe. Our solution elucidates the dependence of the pipe height and the surface tension distribution on the governing parameters.

5.1. Entry pipe flow

Consider the flow at the entrance of a rigid pipe. We assume that across the mouth of the pipe ($z = 0$), the jet has uniform speed V . As the flow proceeds into the pipe, a viscous boundary layer of width $\delta(z)$ develops along the pipe wall. Outside the boundary layer ($0 \leq r \leq a - \delta$), the flow has an approximately flat profile $u(r, z) \approx U(z)$. The flow inside the boundary layer evolves according to the continuity equation and the boundary layer approximation of the z -momentum equation, respectively,

$$\frac{\partial u}{\partial z} + \frac{1}{r} \frac{\partial}{\partial r}(rv) = 0, \tag{5.1}$$

$$u \frac{\partial u}{\partial z} + v \frac{\partial u}{\partial r} = -\frac{1}{\rho} \frac{dp}{dz} + \frac{v}{r} \frac{\partial}{\partial r} \left(r \frac{\partial u}{\partial r} \right), \tag{5.2}$$

where p is the fluid pressure. According to the boundary layer approximation, $dp/dr \approx 0$; hence, $p = p(z)$. The volume flux through any pipe cross-section is constant,

$$Q = 2\pi \int_0^a ur \, dr = \pi a^2 V, \tag{5.3}$$

and the flow vanishes on the pipe walls

$$u = v = 0, \quad r = a. \tag{5.4}$$

Equations (5.1)–(5.4) can be integrated to yield the momentum and energy integral equations (Campbell & Slattery 1963):

$$\rho \frac{d}{dz} \int_0^a u^2 r \, dr + \frac{a^2}{2} \frac{dp}{dz} - a\mu \left. \frac{\partial u}{\partial r} \right|_{r=a} = 0, \tag{5.5}$$

$$\frac{dp}{dz} \frac{a^2 V}{2} + \frac{\rho}{2} \frac{d}{dz} \int_0^a u^3 r \, dr + \mu \int_0^a \left(\frac{\partial u}{\partial r} \right)^2 r \, dr = 0. \tag{5.6}$$

Eliminating dp/dz from (5.5) and (5.6) gives

$$\frac{1}{2} \frac{d}{dz} \int_0^a u^3 r \, dr + v \int_0^a \left(\frac{\partial u}{\partial r} \right)^2 r \, dr = V \frac{d}{dz} \int_0^a u^2 r \, dr - avV \left. \frac{\partial u}{\partial r} \right|_{r=a}. \tag{5.7}$$

Henceforth, we redefine the dimensional variables z , r , u and p as z' , r' , u' and p' , respectively, and define the dimensionless variables

$$s = \frac{\delta}{a}, \quad z = \frac{z'}{H}, \quad r = \frac{r'}{a}, \quad u = \frac{u'}{V}. \quad (5.8)$$

Equations (5.3) and (5.7) then assume the dimensionless form

$$\int_0^1 ur \, dr = \frac{1}{2}, \quad (5.9)$$

$$\frac{aRe}{H} \frac{ds}{dz} \frac{d}{ds} \left(\frac{1}{2} \int_0^1 u^3 r \, dr - \int_0^1 u^2 r \, dr \right) = - \int_0^1 \left(\frac{\partial u}{\partial r} \right)^2 r \, dr - \left. \frac{\partial u}{\partial r} \right|_{r=1}. \quad (5.10)$$

5.2. Flow in a fluid pipe

Consider a vertical axisymmetric water jet falling under the influence of gravity with an upward surface stress applied at the jet surface (figure 3). Guided by our experimental observations, we assume that the fluid pipe is characterized by a constant radius a and a vanishing surface velocity. As in simple entry pipe flow, a viscous boundary layer of width δ separates the jet surface from an inviscid core region; δ increases with distance downstream, but does not entirely span the fluid pipe before the jet impinges on the reservoir.

The flow in a vertical axisymmetric fluid pipe is governed by the same equations (5.1)–(5.4) relevant for entry pipe flow provided the fluid pressure p' is replaced by the dynamic pressure p'_d :

$$p'_d = p' - \rho g z'. \quad (5.11)$$

Furthermore, normal and tangential stress boundary conditions must be satisfied on the fluid pipe surface. On the cylindrical pipe surface of radius a , when $Re \gg 1$ these assume the simple form

$$p'(z') = p_a + \frac{\sigma'(z')}{a}, \quad (5.12)$$

$$\mu \left. \frac{\partial u'}{\partial r'} \right|_{r'=a} = \frac{d\sigma'}{dz'}, \quad (5.13)$$

where p_a is ambient pressure and σ' the surface tension.

Setting $r' = a$ in the momentum equation (5.2) and using (5.11)–(5.13) yields

$$\left[\frac{1}{a} \frac{\partial u'}{\partial r'} + \frac{\partial^2 u'}{\partial r'^2} \right]_{r'=a} = \frac{1}{\mu} \frac{dp'_d}{dz'} = \frac{1}{a} \left. \frac{\partial u'}{\partial r'} \right|_{r'=a} - \frac{g}{v}. \quad (5.14)$$

Simplification yields a single boundary condition for u' :

$$\left. \frac{\partial^2 u'}{\partial r'^2} \right|_{r'=a} = -\frac{g}{v}. \quad (5.15)$$

In the dimensionless variables defined in (5.8), (5.15) becomes

$$\left. \frac{\partial^2 u}{\partial r^2} \right|_{r=1} = -\mathcal{S}^{-1}, \quad (5.16)$$

where the Stokes number, $\mathcal{S} = vV/(ga^2)$, prescribes the relative importance of viscous and gravitational forces. The free-surface boundary condition (5.16) underlines the difference between flow in a fluid pipe and simple entry pipe flow.

5.3. Approximate solution

Van Dyke (1970) and Fargie & Martin (1971) list and review the four principle theoretical approaches to the classical problem of entry pipe flow in the absence of gravity: finite-difference numerical solution (e.g. Langhaar 1942; Friedmann, Gillis & Liron 1968); approximate solution through linearization of inertial terms (e.g. Sparrow, Lin & Lundgren 1964); perturbation series expansions (e.g. Boussinesq 1891; Goldstein 1938); and the Kármán–Polhausen integral methods (e.g. Schiller 1922; Campbell & Slattery 1963). Of these four approaches, the latter is the most simply adapted to the problem of interest, in which the complicating influence of gravity and the free surface on the boundary layer dynamics must be considered explicitly.

In the Kármán–Polhausen models, entry pipe flow is described as an inviscid core plug flow being encroached upon by a developing laminar boundary layer with a polynomial velocity profile. The polynomial profile satisfies a chosen set of integral equations derived from the continuity and momentum equations. For the entry pipe flow problem, different authors (e.g. Campbell & Slattery 1963; Fargie & Martin 1971; Gupta 1977; Mohanty & Asthana 1978) have used different polynomial profiles, imposed different integral conditions, and deduced slightly different solutions. When the various approaches were applied to our problem, we found that remarkably similar results were obtained. As the results of Campbell & Slattery (1963) have been extensively benchmarked against the asymptotic theories of Boussinesq (1891) and Goldstein (1938), Langhaar’s (1942) approximate solution via linearization of inertial terms, the Kármán–Polhausen solution of Schiller (1922), and a great deal of experimental data, we here adapt their formulation to the problem of interest.

In dimensionless variables, the flow profile is approximated as

$$u(r, z) = \begin{cases} U(z), & 0 \leq r < 1 - s, \\ U(z) \sum_{n=0}^5 A_n(z) \eta^n, & 1 - s \leq r \leq 1, \end{cases} \quad (5.17)$$

where $\eta = (1 - r)/s$ is the dimensionless boundary layer variable and $U(z)$ represents the plug flow speed in the inviscid core. The coefficients $A_n(z)$, the dimensionless boundary layer thickness $s(z)$ and the outer flow $U(z)$ are determined by imposing the integral relation (5.10), the boundary conditions (5.4) and (5.16), the volume flux condition (5.9), and by forcing u to match the outer flow profile $U(z)$ smoothly. Specifically, we require that $u = U$ and $d^n u/dr^n = 0$ for $n = 1, 2, 3$ at $r = 1 - s$ in order to ensure the consistency of our solution over the parameter regime examined experimentally. Straightforward algebra yields the boundary layer profile

$$u = U(z) \eta \left(2 - \eta + (1 - \eta)^2 + (1 - \eta)^3 - \left(\frac{3}{2} - \frac{s^2}{8\mathcal{S}U(z)} \right) (1 - \eta)^4 \right), \quad (5.18)$$

where the core velocity is given by

$$U(z) = \frac{840 - \mathcal{S}^{-1}s^3(7 - 2s)}{20(42 - 21s + 4s^2)}. \quad (5.19)$$

The evolution of the dimensionless boundary layer thickness $s(z)$ is prescribed by

$$\frac{H}{aRe} \frac{dz}{ds} = \frac{sF(s, \mathcal{S})}{G(s, \mathcal{S})} \frac{420 - \mathcal{S}^{-1}s^2(s^2 - 7s + 21)}{(4s^2 - 21s + 42)^2}, \quad (5.20)$$

where $F(s, \mathcal{S})$ and $G(s, \mathcal{S})$ are listed in Appendix B.

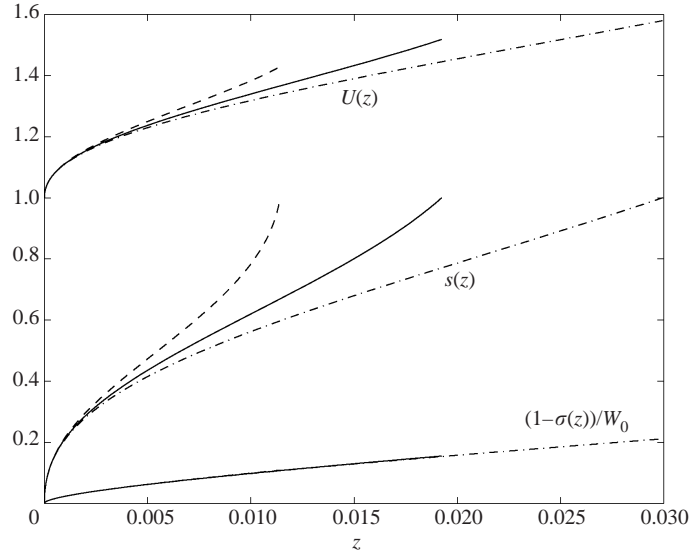


FIGURE 7. Theoretically predicted z -dependence of the scaled surface tension deficit $(1 - \sigma(z))/W_0 = (\sigma_0 - \sigma')/(\Delta\sigma W_d)$, boundary layer thickness $s(z)$ and inviscid core velocity $U(z)$ for Stokes numbers $\mathcal{S} = \nu V/(ga^2) = 0.04$ (dashed line), 0.062 (solid line) and 0.1 (dash-dot line) that span the experimental parameter regime.

We assume the surface tension at the top of the fluid pipe is that of the incoming water, $\sigma'(0) = \sigma_0$, while the surface tension at the bottom of the fluid pipe, $z' = H$, is that of the reservoir, $\sigma'(H) = \sigma_1$. We define the dimensionless surface tension as $\sigma = \sigma'/\sigma_0$. The tangential stress boundary condition (5.13) yields an equation governing $\sigma(z)$,

$$\frac{aRe}{H} \frac{d\sigma}{dz} = -W_0 \frac{420 + \mathcal{S}^{-1}s^2(21 - 14s + 3s^2)}{4s(4s^2 - 21s + 42)}, \quad (5.21)$$

where $W_0 = \rho a V^2/\sigma_0$. Combining (5.20) and (5.21) yields the variation of surface tension with boundary layer thickness:

$$\frac{d\sigma}{ds} = -W_0 \frac{F(s, \mathcal{S})}{G(s, \mathcal{S})} \frac{(420 + \mathcal{S}^{-1}s^2(21 - 14s + 3s^2))(420 - \mathcal{S}^{-1}s^2(s^2 - 7s + 21))}{4(4s^2 - 21s + 42)^3}. \quad (5.22)$$

From (5.20) and (5.22), the evolution of $s(z)$ and $\sigma(z)$ from their initial values, $s = 0$ and $\sigma = 1$ at $z = 0$, may thus be traced. The profiles so obtained of $s(z)$, $U(z)$ and $\sigma(z)$ are plotted in figure 7. While $s(z)$ and $U(z)$ vary noticeably with \mathcal{S} , $\sigma(z)$ is virtually independent of \mathcal{S} . Finally, we note that if the equation of state relating surface tension σ to surfactant concentration is known, the distribution of surfactant along the fluid pipe may also be determined.

A useful check of our theory is to calculate the limiting behaviour of $U(z)$, $s(z)$ and $\sigma(z)$ near the top of the pipe, where $(z, s) \ll 1$. In this limit, (5.19), (5.20) and (5.22) become, respectively,

$$U = 1 + \frac{s}{2}, \quad \frac{H}{aRe} \frac{dz}{ds} = 0.0294 s, \quad \frac{d\sigma}{ds} = -0.0734 W_0, \quad (5.23)$$

where numerical coefficients have been rounded to three significant digits. Integrating the last two equations, applying the boundary conditions at $z = 0$, and manipulat-

ing yields

$$U(z) = 1 + 4.13\sqrt{\frac{Hz}{aRe}}, \quad s(z) = 8.25\sqrt{\frac{Hz}{aRe}}, \quad \sigma(z) = 1 - 0.606 W_0\sqrt{\frac{Hz}{aRe}}. \quad (5.24)$$

The model captures the well-known dependence of U and s on \sqrt{z} that arises in the Blasius profile (Schlichting 1987).

5.4. Pipe height

Integrating (5.20) and (5.22) and applying the boundary conditions gives

$$\frac{H}{aRe} = \int_0^{s_1} \frac{sF(s, \mathcal{S})}{G(s, \mathcal{S})} \frac{420 - \mathcal{S}^{-1}s^2(s^2 - 7s + 21)}{(4s^2 - 21s + 42)^2} ds, \quad (5.25)$$

$$\frac{1}{W_d} = \int_0^{s_1} \frac{F(s, \mathcal{S})}{G(s, \mathcal{S})} \frac{(420 + \mathcal{S}^{-1}s^2(21 - 14s + 3s^2))(420 - \mathcal{S}^{-1}s^2(s^2 - 7s + 21))}{4(4s^2 - 21s + 42)^3} ds, \quad (5.26)$$

where s_1 is the scaled boundary layer thickness at the base of the pipe. Given \mathcal{S} and W_d , the scaled fluid pipe height $H/(aRe)$ is found by first solving (5.26) for s_1 , and then (5.25) for $H/(aRe)$. The height of the fluid pipe $H/(aRe)$ thus depends exclusively on two dimensionless parameters: W_d and \mathcal{S} .

Theoretical predictions for the pipe height based on (5.25) and (5.26) are presented in figure 8 along with our experimental data. We note that $H/(aRe)$ depends only weakly on \mathcal{S} in the parameter regime of interest. In our experiments, \mathcal{S} varied between 0.04 and 0.1; the corresponding theoretical curves indicating the dependence of pipe height on W_d are virtually indistinguishable. Consequently, we plot the curve for the mean experimental value $\mathcal{S} = 0.062$. The data are well-described by our theoretical predictions over the full range of parameters explored.

5.5. Asymptotic forms

We proceed by deriving the asymptotic forms of (5.25) and (5.26) in the limit of $\varepsilon \equiv \sqrt{H/(aRe)} \ll 1$, and so deduce simple algebraic expressions for $H(W_d, \mathcal{S})$. We note that in our experiments, ε lies in the range 0.03–0.13 (see figure 8). We introduce the scaled quantities

$$\hat{\mathcal{S}} = \frac{\mathcal{S}}{\varepsilon}, \quad \hat{s} = \frac{s}{\varepsilon}, \quad \hat{W}_d = \varepsilon W_d. \quad (5.27)$$

In the parameter regime considered experimentally, $\hat{\mathcal{S}}$ ranges from 0.25 to 2.5; moreover, Schlichting's result (2.2) indicates that $s \sim \varepsilon$, while (2.3) requires that $W_d \sim \varepsilon^{-1}$. Consequently, $\hat{\mathcal{S}}$, \hat{s} and \hat{W}_d are all $O(1)$ quantities. Note that \mathcal{S}^{-1} is $O(\varepsilon^{-1})$; however, it always appears in (5.25) and (5.26) as the product $\mathcal{S}^{-1}s^2$, which is $O(\varepsilon)$. Thus the effect of gravity, as introduced through \mathcal{S} , is an $O(\varepsilon)$ effect in our asymptotic theory. Substituting (5.27) into (5.25), evaluating the integral, substituting $\hat{s}_1 = \hat{s}_{10} + \varepsilon\hat{s}_{11} + O(\varepsilon^2)$ and equating like powers of ε yields

$$\hat{s}_{10} = 8.25, \quad \hat{s}_{11} = -91.6 + 24.1\hat{\mathcal{S}}^{-1}. \quad (5.28)$$

Substituting (5.27) and (5.28) into (5.26), evaluating the integral, squaring the result and retaining $O(\varepsilon)$ terms yields

$$\frac{2.73}{\hat{W}_d^2} = 1 + \varepsilon(15.2 + 0.323\hat{\mathcal{S}}^{-1}). \quad (5.29)$$

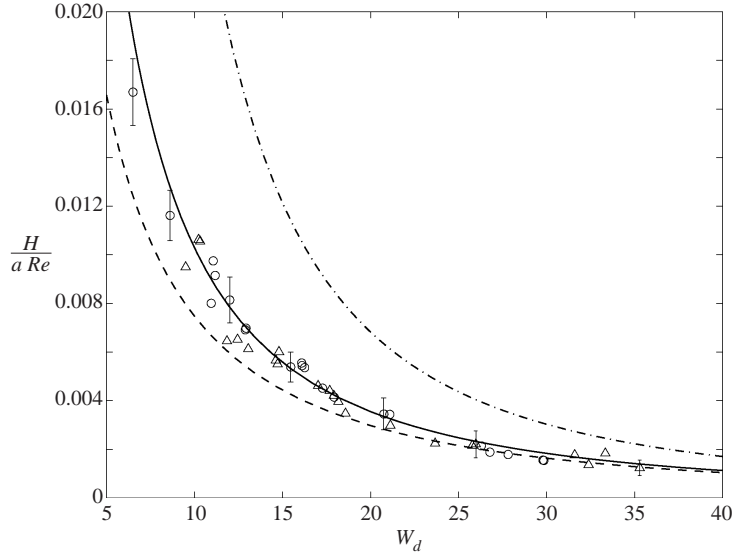


FIGURE 8. Observed dependence of dimensionless fluid pipe height $H/(aRe)$ on dynamic Weber number $W_d = \rho a V^2 / \Delta \sigma$ for Ivory (\circ) and Tide (\triangle) surfactants. Characteristic error bars are shown. The solid line represents the predictions for the fluid pipe height (for the mean $\mathcal{S} = vV/(ga^2) = 0.062$) based on the complete theory ((5.25) and (5.26)). The dot-dashed line represents the $O(1)$ asymptotic short-pipe prediction for the dimensionless pipe height, (5.30). The $O(\varepsilon)$ asymptotic prediction, (5.31), is represented by the dashed line.

The leading-order terms of (5.29) imply $W_d^2 \varepsilon^2 = \hat{W}_d^2 = 2.73 + O(\varepsilon)$, or

$$\frac{H}{aRe} = \frac{2.73}{W_d^2}. \quad (5.30)$$

The form of the leading-order result (5.30) is consistent with our original scaling (2.3), in which gravitational effects were neglected. Equation (5.30) indicates that ε and $\hat{\mathcal{S}}^{-1}$ may be replaced by $\sqrt{2.73}/W_d$ and $\sqrt{2.73}/(W_d \mathcal{S})$, respectively, in the $O(\varepsilon)$ term of (5.29) while still retaining $O(\varepsilon)$ accuracy. Making these replacements and suitable rearrangement yields

$$\frac{H}{aRe} = \frac{2.73}{W_d^2} \left(1 + \frac{25.1}{W_d} + \frac{0.879}{\mathcal{S} W_d^2} \right)^{-1}. \quad (5.31)$$

Equation (5.31) contains an $O(\varepsilon)$ correction to (5.30) which includes the first effects of gravity.

The $O(1)$ and $O(\varepsilon)$ asymptotic approximations, respectively (5.30) and (5.31), are plotted in figure 8 along with the full theoretical predictions (5.25) and (5.26). We note that the asymptotic solutions are expected to be valid only for $\varepsilon \ll 1$ and $W_d \gg 1$. While the asymptotic solutions are thus not strictly valid over the entire experimental parameter range, the $O(\varepsilon)$ solution (5.31) provides a reasonable approximation to the full theory.

6. Discussion and conclusions

By integrating the existing theoretical model of a free-falling jet with a suitably modified model of entry flow into a rigid pipe, we have deduced a theoretical

description of the fluid pipe. An accompanying experimental study indicates that the pipe height depends on the governing parameters in a manner prescribed by our theoretical model. We have also presented new experimental measurements of jet profiles and wavelengths of capillary waves excited in the region adjoining a clean reservoir.

The fluid pipe is an example of a gravity-driven flow in which surfactants serve to suppress surface motions. Such is also the case in the draining rigid soap film (Mysels, Shinoda & Frankel 1959); however, the flow within soap films is dominated by the influence of fluid viscosity. The ability of surfactant to suppress surface motions in compactional flows is also evident when wind blows over a puddle: the wind stress causes surfactant to accumulate at the leeward side of the puddle, where a quiescent surface region void of waves may be observed. Impurities also accumulate in the vicinity of stagnation points upstream of obstacles in rivers, giving rise to a locally stagnant surface region. The collision of the incoming flow with the surfactant-laden stagnant region results in the margins of the latter being marked by a pronounced surface deflection known as the Reynolds ridge (McCutchen 1970; Harper & Dixon 1974; Scott 1982; Jensen 1998). While an axisymmetric Reynolds ridge may well exist at the top of the fluid pipe, it is not readily discernible owing to the presence of the capillary wave field.

Surfactants may have an important impact on the rate of mass transfer into falling jets and films as arise, for example, in wetted-wall column absorbers (Emmert & Pigford 1954; Lynn, Straatemeier & Kramers 1955). Surfactants typically diminish mass transfer across an interface through their influence on surface chemistry (e.g. Sada & Himmelblau 1967). Moreover, the rate of gas absorption in falling jets and films is known to be enhanced by the presence of capillary waves (Nieuwoudt & Crause 1999); consequently, surfactants may further diminish absorption rates through suppressing capillary waves. Finally, the addition of a soluble surfactant to a falling film may render the film unstable to Marangoni convection, thus enhancing mass transfer across its surface (Ji & Setterwall 1994, 1995). Evidently, the influence of surfactant on mass transfer across falling films and jets depends explicitly on the type and concentration of surfactant. We have developed a detailed theoretical description of the dynamic influence of surfactants on fluid jets impinging on a reservoir saturated with an insoluble surfactant.

It is a noteworthy experimental observation that only surfactants with an insoluble or sparingly soluble component (in particular, the commercial detergents Tide and Ivory) produce fluid pipes with the stagnant surfaces described by our theory. Surfactants with higher solubility, such as SDS, give rise to pipe-like structures marked by convective motions on their surface. Presumably, as the surfactant desorbs from the surface into the bulk, a static balance between viscous and Marangoni stresses is no longer tenable, and Marangoni convection is prompted on the pipe surface. Similar unsteady pipe structures arise when a water jet impinges on a reservoir of alcohol. In this case, while a Marangoni stress between reservoir and jet is again established, the dynamics are more complicated and some combination of diffusion and evaporation of alcohol evidently precludes the possibility of a stagnant fluid pipe.

Finally, for the sake of completeness, in Appendix C we present a theoretical description of the two-dimensional analogue of the fluid pipe, which may arise when a fluid sheet impinges on a contaminated reservoir and take the form of a stagnant planar region adjoining the reservoir. The scaling of the planar pipe is identical to (2.3) when the cylindrical pipe radius a is replaced by the planar pipe half-width a .

The authors thank Tony Howes for drawing this problem to our attention. We also gratefully acknowledge Gareth McKinley for granting us access to his surface-tensiometer, and Alex Hasha for his assistance with the experiments. Finally, we thank Harvey Greenspan, Manoj Chaudhury and Randal Hill for a number of valuable discussions.

Appendix A. Capillary waves

The capillary waves supported by a falling pure water jet are described as infinitesimal axisymmetric disturbances

$$\xi = \hat{\xi}(z) e^{i(kz - \omega t)} \quad (\text{A } 1)$$

on the base radial profile $a(z)$, so that the instantaneous radial profile is $a(z, t) = a(z) + \xi(z, t)$. Rayleigh (1879, 1892) derived the dispersion relation for waves on a cylindrical inviscid jet in the absence of gravity ($a(z) = a_0$, $\hat{\xi} = \text{constant}$):

$$\frac{\omega^2}{k^2} = \frac{\sigma_0}{\rho a_0} \frac{I_1(\alpha)}{I_0(\alpha)} \left(\alpha - \frac{1}{\alpha} \right), \quad \alpha = |k|a_0, \quad (\text{A } 2)$$

where I_0 and I_1 are modified Bessel functions of the first kind of order zero and one, respectively. The analogous relation for the case of a viscous jet was also derived by Rayleigh (1892). With parameters relevant to our experimental study, the capillary wavelengths predicted by the inviscid and viscous theories are indistinguishable; hence, the effects of viscosity may again be safely neglected.

To apply Rayleigh's theory to a vertical water jet, we note that the jet profile varies slowly in z . In the jet frame of reference, the amplitude of the capillary waves is proportional to $e^{i(kz - \omega t)}$, where $\omega > 0$. Since the waves are stationary in the lab frame, their phase speed must be equal and opposite to the local jet speed, $U = -\omega/k$. Setting $U^2(z) = \omega^2/k^2$ and replacing a_0 with the local jet radius $a(z)$ in (A 2) gives

$$U^2 = \frac{\omega^2}{k^2} = \frac{\sigma}{\rho a} \frac{I_1(\alpha)}{I_0(\alpha)} \left(\alpha - \frac{1}{\alpha} \right), \quad (\text{A } 3)$$

where $\alpha = |k|a(z)$. A similar result was derived by Anno (1977). In the parameter regime considered experimentally, the jet profiles are described within experimental error by (4.5) (figure 6). Therefore, for the sake of simplicity, (4.5), rather than (4.3) and (4.4), is used to calculate the velocity and radial profiles for our base flows. Substituting (4.5) into (A 3) yields

$$\frac{I_1(\alpha)}{I_0(\alpha)} \left(\alpha - \frac{1}{\alpha} \right) = W_0(\Pi + 1)^{3/4}. \quad (\text{A } 4)$$

The predicted dependence of the wavelength λ on height z is thus

$$\frac{\lambda}{a_0} = \frac{2\pi a/a_0}{\alpha(W_0, \Pi)} = \frac{2\pi(\Pi + 1)^{-1/4}}{\alpha(W_0, \Pi)}. \quad (\text{A } 5)$$

Figure 9 indicates that the observed capillary wavelengths are reasonably well-described, but systematically greater than those predicted by (A 4) and (A 5). The discrepancy probably results from finite-amplitude effects on the wave field.

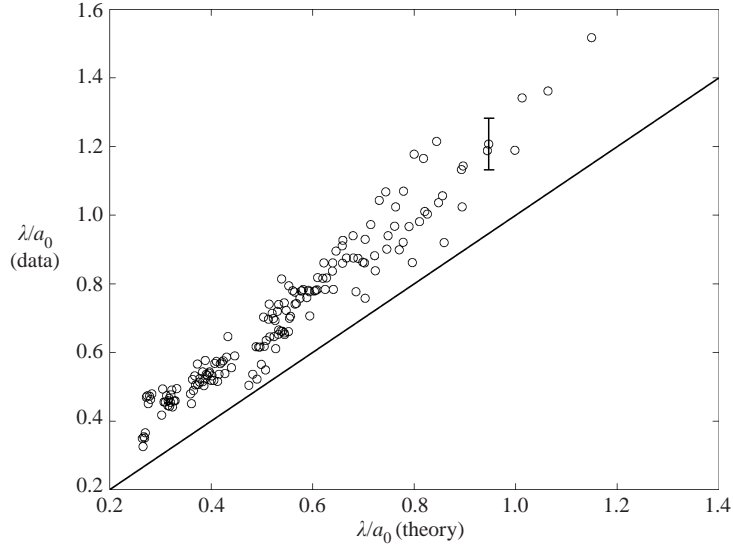


FIGURE 9. Comparison of observed and theoretically predicted dimensionless capillary wavelengths λ/a_0 . The theoretical wavelength is found by substituting the local values of $\Pi = 2g(z + z_0)/U_0^2$ and $W_0 = \rho a_0 U_0^2/\sigma_0$ into (A 4) and (A 5). A characteristic error bar is shown.

Appendix B

The functions $F(s, \mathcal{S})$ and $G(s, \mathcal{S})$ arising in § 5.3 and § 5.4 are given by

$$\begin{aligned}
 F(s, \mathcal{S}) = & \frac{1421637}{9152} + \frac{210226317}{777920}s - \frac{10317503}{14144}s^2 + \frac{4782127}{9724}s^3 - \frac{2751}{22}s^4 + \frac{1706}{165}s^5 \\
 & + \frac{\mathcal{S}^{-1}s^2}{91520} \left(166845 - \frac{191077607}{85}s + \frac{326905159}{85}s^2 - \frac{664814962}{255}s^3 \right. \\
 & \left. + \frac{206471897}{255}s^4 - \frac{9697992}{85}s^5 + \frac{21008}{3}s^6 - \frac{832}{3}s^7 \right) \\
 & + \frac{\mathcal{S}^{-2}s^4}{66560} \left(-9261 + \frac{32343969}{935}s - \frac{44432801}{935}s^2 + \frac{1752492}{55}s^3 \right. \\
 & \left. - \frac{31516957}{2805}s^4 + \frac{114891}{55}s^5 - \frac{183977}{935}s^6 + \frac{167392}{19635}s^7 \right), \quad (\text{B } 1)
 \end{aligned}$$

$$\begin{aligned}
 G(s, \mathcal{S}) = & 1260 - \frac{3255}{2}s + 420s^2 + \mathcal{S}^{-1}s^2 \left(168 - \frac{749}{4}s + \frac{403}{4}s^2 - \frac{167}{6}s^3 + 3s^4 \right) \\
 & + \frac{\mathcal{S}^{-2}s^4}{4} \left(-7 + \frac{77}{8}s - \frac{71}{12}s^2 + \frac{19}{10}s^3 - \frac{121}{420}s^4 + \frac{11}{840}s^5 \right). \quad (\text{B } 2)
 \end{aligned}$$

Appendix C. Planar pipes

The theoretical description of flow in a planar fluid pipe (or rectangular duct) closely follows that in the cylindrical geometry. The physical picture is the same as shown in figure 3: a boundary layer of thickness $\delta(z)$ grows along the sides of the

planar pipe. We denote by v' the velocity component in the y -direction, and by y' the cross-channel coordinate, so that $y' = \pm a$ denote the pipe boundaries.

The flow in the boundary layer is governed by the continuity and boundary layer axial momentum equations:

$$\frac{\partial u'}{\partial z'} + \frac{\partial v'}{\partial y'} = 0, \quad u' \frac{\partial u'}{\partial z'} + v' \frac{\partial u'}{\partial y'} = -\frac{1}{\rho} \frac{dp'}{dz'} + \nu \frac{\partial^2 u'}{\partial y'^2}. \quad (\text{C } 1)$$

The flow vanishes at the pipe walls. The normal stress balance assumes the form $p'(z') = p_a$. The boundary conditions (5.13) and (5.15) are still valid with r' replaced by y' .

We define the dimensionless variables s , z and u as in (5.8), and $y = y'/a$. From (C 1) and the boundary conditions listed above, we derive an equation analogous to the integral equation (5.10),

$$\frac{aRe}{H} \frac{ds}{dz} \frac{d}{ds} \left(\frac{1}{2} \int_0^1 u^3 dy - \int_0^1 u^2 dy \right) = - \int_0^1 \left(\frac{\partial u}{\partial y} \right)^2 dy - \left. \frac{\partial u}{\partial y} \right|_{y=1}. \quad (\text{C } 2)$$

The dimensionless constant volume flux condition for the planar flow is

$$\int_0^1 u dy = 1. \quad (\text{C } 3)$$

The flow profile in the boundary layer is approximated by (5.17), with $\eta = (1-y)/s$. To resolve the unknowns $A_n(z)$, $s(z)$ and $U(z)$, we impose the integral relation (C 2), the volume flux condition (C 3) and the boundary conditions (5.4) and (5.16), with r replaced by y . At $y = 1 - s$, we impose the same degree of smoothness on u as in the cylindrical case. The approximate profile still has the form (5.18), but $U(z)$ is now given by

$$U(z) = \frac{240 - \mathcal{S}^{-1}s^3}{60(4-s)}. \quad (\text{C } 4)$$

The variation of the scaled boundary layer thickness s is governed by

$$\frac{H}{aRe} \frac{dz}{ds} = \frac{504 s F_p(s, \mathcal{S})}{G_p(s, \mathcal{S})} \frac{120 - \mathcal{S}^{-1}s^2(6-s)}{(4-s)^2}, \quad (\text{C } 5)$$

where

$$\begin{aligned} F_p(s, \mathcal{S}) = & \frac{1}{2970} \left(\frac{48355}{364} + \frac{103683}{728}s - 139s^2 \right) \\ & + \frac{\mathcal{S}^{-1}s^2}{64864800} (34050 - 232969s + 143541s^2 - 4550s^3) \\ & + \frac{\mathcal{S}^{-2}s^4}{518918400} (-20790 + 36033s - 16496s^2 + 1043s^3), \end{aligned} \quad (\text{C } 6)$$

$$G_p(s, \mathcal{S}) = 5760 - 5040s + 12\mathcal{S}^{-1}s^2(64 - 34s + 7s^2) - \mathcal{S}^{-2}s^4(8 - 5s + s^2). \quad (\text{C } 7)$$

The variation of the scaled surface tension $\sigma = \sigma'/\sigma_0$ in terms of s is deduced from (5.13) and (C 5),

$$\frac{d\sigma}{ds} = -W_0 \frac{F_p(s, \mathcal{S})}{G_p(s, \mathcal{S})} \frac{84(60 + \mathcal{S}^{-1}s^2(3-s))(120 - \mathcal{S}^{-1}s^2(6-s))}{(4-s)^3}. \quad (\text{C } 8)$$

Integrating (C 5) and (C 8) from $s = 0$ to $s = s_1$ and imposing the same boundary conditions as in the cylindrical case yields

$$\frac{H}{aRe} = \int_0^{s_1} \frac{504 s F_p(s, \mathcal{S})}{G_p(s, \mathcal{S})} \frac{120 - \mathcal{S}^{-1} s^2 (6 - s)}{(4 - s)^2} ds, \quad (\text{C } 9)$$

$$\frac{1}{W_d} = \int_0^{s_1} \frac{F_p(s, \mathcal{S})}{G_p(s, \mathcal{S})} \frac{84(60 + \mathcal{S}^{-1} s^2 (3 - s))(120 - \mathcal{S}^{-1} s^2 (6 - s))}{(4 - s)^3} ds. \quad (\text{C } 10)$$

The numerical procedure to find the scaled pipe height $H/(aRe)$ from (C 9) and (C 10) follows as previously.

A simple relation for short pipes ($\varepsilon \ll 1$) is found by proceeding as for the case of cylindrical pipes. Equation (5.27) and the expansion $\widehat{s}_1 = \widehat{s}_{10} + \varepsilon \widehat{s}_{11} + O(\varepsilon^2)$ are substituted into (C 9) and (C 10), the integrals are computed and \widehat{s}_{10} , \widehat{s}_{11} are found and substituted back into the results. Retaining only $O(\varepsilon^0)$ terms in this calculation yields (5.30). Retaining $O(\varepsilon)$ terms throughout the calculation yields the dependence of planar pipe height on the governing parameters:

$$\frac{H}{aRe} = \frac{2.73}{W_d^2} \left(1 + \frac{14.5}{W_d} + \frac{0.879}{\mathcal{S} W_d^2} \right)^{-1}. \quad (\text{C } 11)$$

REFERENCES

- ADACHI, K. 1987 Laminar jets of a plane liquid sheet falling vertically in the atmosphere. *J. Non-Newtonian Fluid Mech.* **24**, 11–30.
- ANNO, J. N. 1977 *The Mechanics of Liquid Jets*. Lexington, Massachusetts: Lexington Books, D.C. Heath and Company.
- AWATI, K. M. & HOWES, T. 1996 Stationary waves on cylindrical fluid jets. *Am. J. Phys.* **64**, 808–811.
- BIRD, R. B., ARMSTRONG, R. C. & HASSAGER, O. 1987 *Dynamics of Polymeric Liquids*, 2nd Edn, Vol. I. *Fluid Mechanics*. John Wiley & Sons.
- BOUSSINESQ, J. 1891 Sur la manière dont les vitesses, dans un tube cylindrique de section circulaire, évase à son entrée, se distribuent depuis cette entrée jusqu'aux endroits où se trouve établi un régime uniforme. *Comptes Rendus* **113**, 9–15, 49–51.
- BRUN, R. F. & LIENHARD, J. H. 1968 Behavior of free laminar jets leaving Poiseuille tubes. *ASME Paper* 68-FE-44.
- CAMPBELL, W. D. & SLATTERY, J. C. 1963 Flow in the entrance of a tube. *Trans. ASME: J. Basic Engng* **33**, 41–46.
- CLARKE, N. S. 1968 Two-dimensional flow under gravity in a jet of viscous liquid. *J. Fluid Mech.* **31**, 481–500.
- CLARKE, N. S. 1969 The asymptotic effects of surface tension and viscosity on an axially-symmetric free jet of liquid under gravity. *Q. J. Mech. Appl. Maths* **22**, 247–256.
- CULLEN, E. J. & DAVIDSON, J. F. 1957 Absorption of gases in liquid jets. *Trans. Faraday Soc.* **53**, 113–121.
- DRAZIN, P. G. & REID, W. H. 1981 *Hydrodynamic Stability*. Cambridge University Press.
- DUDA, J. L. & VRENTAS, J. S. 1967 Fluid mechanics of laminar liquid jets. *Chem. Engng Sci.* **22**, 855–869.
- EMMERT, R. E. & PIGFORD, R. L. 1954 A study of gas absorption in falling liquid films. *Chem. Engng Prog.* **50**, 87–93.
- FARGIE, D. & MARTIN, B. W. 1971 Developing laminar flow in a pipe of circular cross-section. *Proc. R. Soc. Lond. A* **321**, 461–476.
- FRIEDMANN, M., GILLIS, J. & LIRON, N. 1968 Laminar flow in a pipe at low and moderate Reynolds numbers. *Appl. Sci. Res.* **19**, 426–438.
- GOLDSTEIN, S. 1938 *Modern Developments in Fluid Dynamics I*. Clarendon Press.
- GONZÁLEZ-MENDIZABAL, D., OLIVERA-FUENTES, C. & GUZMÁN, J. M. 1987 Hydrodynamics of

- laminar liquid jets. Experimental study and comparison with two models. *Chem. Engng Commun.* **56**, 117–137.
- GUPTA, R. C. 1977 Laminar flow in the entrance of a tube. *Appl. Sci. Res.* **33**, 1–10.
- HANSEN, R. S. & AHMAD, J. 1971 Waves at interfaces. *Prog. Surface Membrane Sci.* **4**, 1–55.
- HARPER, J. F. & DIXON, J. N. 1974 The leading edge of a surface film on contaminated flowing water. *Fifth Annual Australasian Conference on Hydraulics and Fluid Mechanics, Christchurch, New Zealand*, pp. 499–505.
- JENSEN, O. E. 1998 The stress singularity in surfactant-driven thin-film flows. Part 2. Inertial effects. *J. Fluid Mech.* **372**, 301–322.
- JI, W. & SETTERWALL, F. 1994 On the instabilities of vertical falling liquid films in the presence of surface-active solute. *J. Fluid Mech.* **278**, 297–323.
- JI, W. & SETTERWALL, F. 1995 Effects of heat transfer additives on the instabilities of an absorbing falling film. *Chem. Engng Sci.* **50**, 3077–3097.
- KAYE, A. & VALE, D. G. 1969 The shape of a vertically falling stream of a Newtonian liquid. *Rheologica Acta* **8**, 1–5.
- LANGHAAR, H. L. 1942 Steady flow in the transition length of a straight tube. *Trans. ASME: J. Appl. Mech.* **9**, 55–58.
- LEVICH, V. G. 1962 *Physicochemical Hydrodynamics*. Prentice-Hall.
- LIENHARD, J. H. 1968 Effects of gravity and surface tension upon liquid jets leaving Poiseuille tubes. *Trans. ASME: J. Basic Engng* **90**, 262–268.
- LUCASSEN-REYNDERS, F. H. & LUCASSEN, J. 1969 Capillary waves. *Adv. Colloid Interface Sci.* **2**, 347–395.
- LYNN, S., STRAATEMEIER, J. R. & KRAMERS, H. 1955 Absorption studies in the light of penetration theory. I. Long wetted-wall columns. *Chem. Engng Sci.* **4**, 49–57.
- MARSHALL, W. R. & PIGFORD, R. L. 1947 *The Application of Differential Equations to Chemical Engineering Problems*. University of Delaware.
- MCCARTHY, M. J. & MALLOY, N. A. 1974 Review of stability of liquid jets and the influence of nozzle design. *Chem. Engng J.* **7**, 1–20.
- MCCUTCHEEN, C. W. 1970 Surface films compacted by moving water: Demarcation lines reveal film edges. *Science* **170**, 61–64.
- MOHANTY, A. K. & ASTHANA, S. B. L. 1978 Laminar flow in the entrance region of a smooth pipe. *J. Fluid Mech.* **90**, 433–447.
- MYSELS, K. J., SHINODA, K. & FRANKEL, S. 1959 *Soap Films, Studies of Their Thinning*. Pergamon.
- NIEUWOUTD, I. & CRAUSE, J. C. 1999 Mass transfer in a short wetted-wall column. 2. Binary systems. *Ind. Engng Chem. Res.* **38**, 4933–4937.
- PETRIE, J. S. 1979 *Elongational Flows*. Pitman.
- PORTER, M. R. 1994 *Handbook of Surfactants*, 2nd Edn. Chapman and Hall.
- RAYLEIGH, LORD 1879 On the instability of jets. *Proc. Lond. Math. Soc.* **10**, 4–13, also in *Scientific Papers* (1899), Vol. I, 361–371, Cambridge University Press.
- RAYLEIGH, LORD 1892 On the stability of a cylinder of viscous liquid under capillary force. *Phil. Mag.* **34**, 145–154.
- SADA, E. & HIMMELBLAU, D. M. 1967 Transport of gases through insoluble monolayers. *AIChE J.* **13**, 860–865.
- SCHILLER, L. 1922 Die entwicklung der laminaren geschwindigkeitsverteilung und ihre bedeutung für zähigkeitmessungen. *Z. Angew. Math. Mech.* **2**, 96–106.
- SCHLICHTING, H. 1987 *Boundary Layer Theory*, 7th Edn. McGraw-Hill.
- SCOTT, J. C. 1982 Flow beneath a stagnant film on water: the Reynolds ridge. *J. Fluid Mech.* **116**, 283–296.
- SCRIVEN, L. E. & PIGFORD, R. L. 1959 Fluid dynamics and diffusion calculations for laminar liquid jets. *AIChE J.* **5**, 397–402.
- SPARROW, E. M., LIN, S. H. & LUNDGREN, T. S. 1964 Flow development in the hydrodynamic entrance region of tubes and ducts. *Phys. Fluids* **7**, 338–347.
- VAN DYKE, M. 1970 Entry flow in a channel. *J. Fluid Mech.* **44**, 813–823.